Cascaded Nano-Optics to Probe Microsecond Atomic Scale Phenomena

Marlous Kamp,[1,2,*,†] Bart de Nijs,[1†] Nuttawut Kongsuwan,[3] Matthias Saba,[3] Rohit Chikkaraddy,[1] Charlie A. Readman,[1] William M. Deacon,[1] Jack Griffiths,[1] Steven J. Barrow,[2] Oluwafemi S. Ojambati,[1] Demelza A. Wright,[1] Junyang Huang,[1] Ortwin Hess,[3] Oren A. Scherman[2,*], Jeremy J. Baumberg[1,*]

[1] NanoPhotonics Centre, Department of Physics, Cambridge University, J J Thomson Avenue, Cambridge CB3 0HE, UK.
[2] Melville Laboratory for Polymer Synthesis, Department of Chemistry, Cambridge University, Lensfield Road, Cambridge CB2 1EW, UK.
[3] The Blackett Laboratory, Department of Physics, Prince Consort Road, Imperial College, London SW7 2AZ, UK.
[†] These authors contributed equally.

*To whom correspondence may be addressed:

- Dr Marlous Kamp
  NanoPhotonics Centre, Department of Physics, Cambridge University, J J Thomson Avenue, Cambridge CB3 0HE, UK.
  Phone:
  Email: mkamp@cantab.net
- Professor Jeremy J. Baumberg
  NanoPhotonics Centre, Department of Physics, Cambridge University, J J Thomson Avenue, Cambridge CB3 0HE, UK.
  Phone: +44 (0)1223 337441
  Email: jjb12@cam.ac.uk
- Professor Oren A. Scherman
  Melville Laboratory for Polymer Synthesis, Department of Chemistry, Cambridge University, Lensfield Road, Cambridge CB2 1EW, UK.
  Phone: +44 (0)1223 334372
  Email: oas23@cam.ac.uk

ORCID identifiers

Marlous Kamp	0000-0003-4915-1312
Bart de Nijs	0000-0002-8234-723X
Nuttawut Kongsuwan	0000-0002-8037-3100
Matthias Saba	0000-0001-5281-4506
Rohit Chikkaraddy	0000-0002-3840-4188
Charlie A. Readman	0000-0001-9743-9180
Steven J Barrow	0000-0001-6417-1800
Demelza A Wright	0000-0002-8854-2714
Junyang Huang	0000-0001-6676-495X
Ortwin Hess	0000-0002-6024-0677
Oren A Scherman	0000-0001-8032-7166
Jeremy J Baumberg	0000-0002-9606-9488

Keywords: Nanophotonics | Nanolensing | Surface-enhanced Raman scattering (SERS) | Few-molecule sensing | Microsecond integration times

ABSTRACT

Plasmonic nanostructures can focus light far below the diffraction limit, and the near thousand-fold field enhancements obtained routinely enable few- and single-molecule detection. However, for processes happening on the molecular scale to be tracked with any relevant time resolution, the emission strengths need to be well beyond what current plasmonic devices provide. Here, we develop hybrid nanostructures incorporating both refractive and plasmonic optics, by creating SiO_2 nanospheres fused to plasmonic nanojunctions. Drastic improvements in Raman efficiencies are consistently achieved, with [single-wavelength] emissions reaching 10^7 counts mW^{-1} s^{-1} and $5 \cdot 10^5$ counts mW^{-1} s^{-1} $molecule^{-1}$, for enhancement factors $>10^{11}$. We demonstrate that such high efficiencies indeed enable tracking of single gold atoms and molecules with 17 µs time resolution, more than a thousand-fold improvement over conventional high-performance plasmonic devices. Moreover, the obtained [integrated] MHz count rates rival (even exceed) those of luminescent sources such as single dye molecules and quantum dots, without bleaching or blinking.

SIGNIFICANCE STATEMENT

Surface enhanced Raman spectroscopy is a powerful analytical technique capable of single molecule sensing. Here, by designing nano-architectures that combine nanoscale lensing and plasmonic coupling, its optical efficiency is improved a thousand-fold. The intense signals we now achieve rival the brightness of conventional single molecule fluorescent dyes and other two-level systems. We demonstrate its capability by resolving the real-time microsecond dynamics of individual gold atoms and lattice defects at room temperature. We also show the ability to detect individual isotopes within ensembles of non-resonant molecules. This step change in signal-to-noise shows the untapped potential of SERS and demonstrates its capability for direct real-time monitoring of chemistry in ambient conditions.

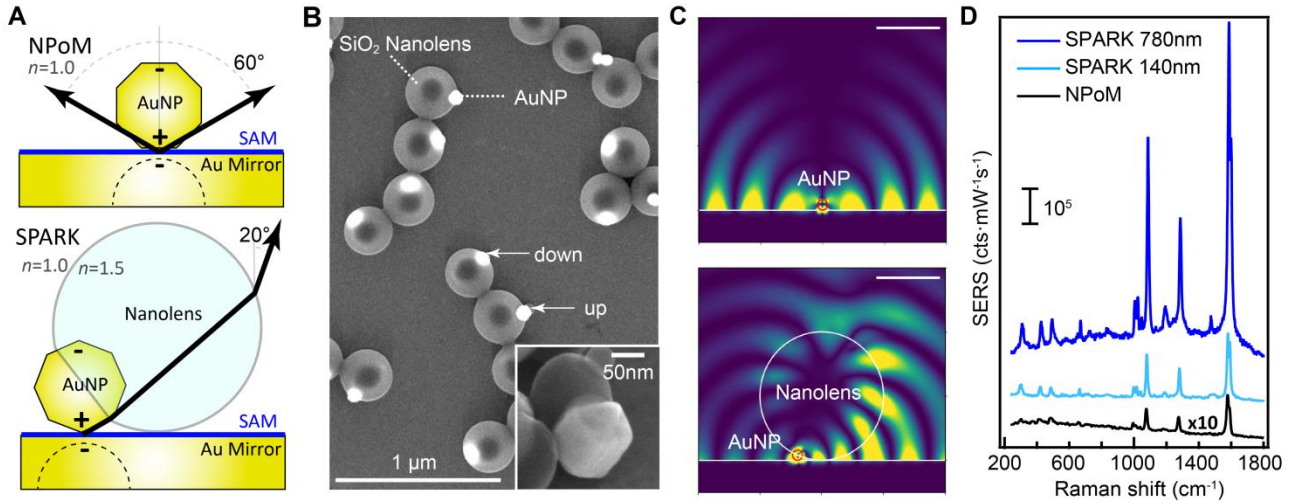

Figure 1 | **SPARK geometries generate ultrahigh SERS efficiencies**. (**A**) Schematic Nanoparticle-on-Mirror (NPoM) (top) and SPARK geometries (bottom) with the nanoparticle 50% embedded into the nanolens. Arrows indicate emission angle of the coupled plasmon mode. (**B**) SEM micrographs showing SPARKs on a gold mirror. (**C**) Snapshots of outcoupling broadband light from a local dipole inside the NPoM (top, 80 nm AuNP) and SPARK (bottom, 80nm AuNP and 800 nm SiO_2) geometries, 15 fs after excitation. Scale bars are 500 nm. (**D**) Typical SERS spectra for a NPoM and two SPARK geometries with nanolens diameters 150,780 nm, using biphenylthiol (BPT) as molecular spacer. NPoM spectrum is scaled x10 and the spectra vertically offset for clarity.

INTRODUCTION

Plasmonic structures are widely used for sensing, on account of their ability to confine light and thus create strong local electromagnetic fields (1). Tremendous effort has been devoted to designing ever better plasmonic nanostructures to maximize these field strengths and thus improve sensing capabilities (2–5). Recently, plasmonic enhancements have been successfully combined with other types of optical confinement, such as the evanescent fields at the surfaces of whispering gallery mode resonators (6) (which have in fact also been used for plasmon-free Raman sensing (7–9)) and the interference maxima provided by Fabry-Pérot cavities (10, 11). Often however, these nanostructures are difficult to fabricate with low yield and high cost. Few studies have exploited nano-refractive elements (12), even though nanoscale spherical lenses are already known to be capable of focussing of light beyond the diffraction limit (13–16) and can thus aid in directing incident light to optimally excite plasmonic hot-spots.

Here, we show that, by combining dielectric nano-optics and plasmonic confinement through simple self-assembly methods into a single colloidal nano-architecture, robust and reproducible Surface-Enhanced Raman Scattering (SERS) enhancement factors exceeding 10^{11} and SERS efficiencies exceeding $5 \cdot 10^5$ counts $mW^{-1}\ s^{-1}$ molecule^{-1} are routinely achieved. Enhancement factors as high as 10^{14} will occasionally be quoted in literature, but none of these high performance SERS substrates show efficiencies anywhere near those observed here (see supplementary materials Table T1). The high optical efficiency and field enhancement allow for spectra to be collected at sub-microWatt laser powers, and provide unrivalled signal-to-noise ratios, reaching $>10^3$ to 1 for only 250 μJ laser dose. To illustrate these improved signal-to-noise ratios, we show it is now possible to detect naturally abundant ^{13}C isotopologues within ensembles of non-resonant molecules. Important for development of surface science, we show that a single atom protrusion or *pico-cavity* induced in the nanogap [which further focusses the field down to a single molecule (17, 18)] allows us to track the behaviour of individual non-resonant molecules and gold atoms in real-time with time resolutions of tens of microseconds. This is fast enough to track single metal atom movements and resolve conformational changes in analytes, making the technique suitable for real-time monitoring of catalytic and chemical reaction processes on a single molecule level. The obtained MHz count rates (cts s^{-1}) vie with (and even exceed) conventional luminescent sources such as single dye molecules and quantum dots used for tagged and tracked emission, with the additional advantage that Raman signals do not exhibit bleaching or blinking (19, 20).

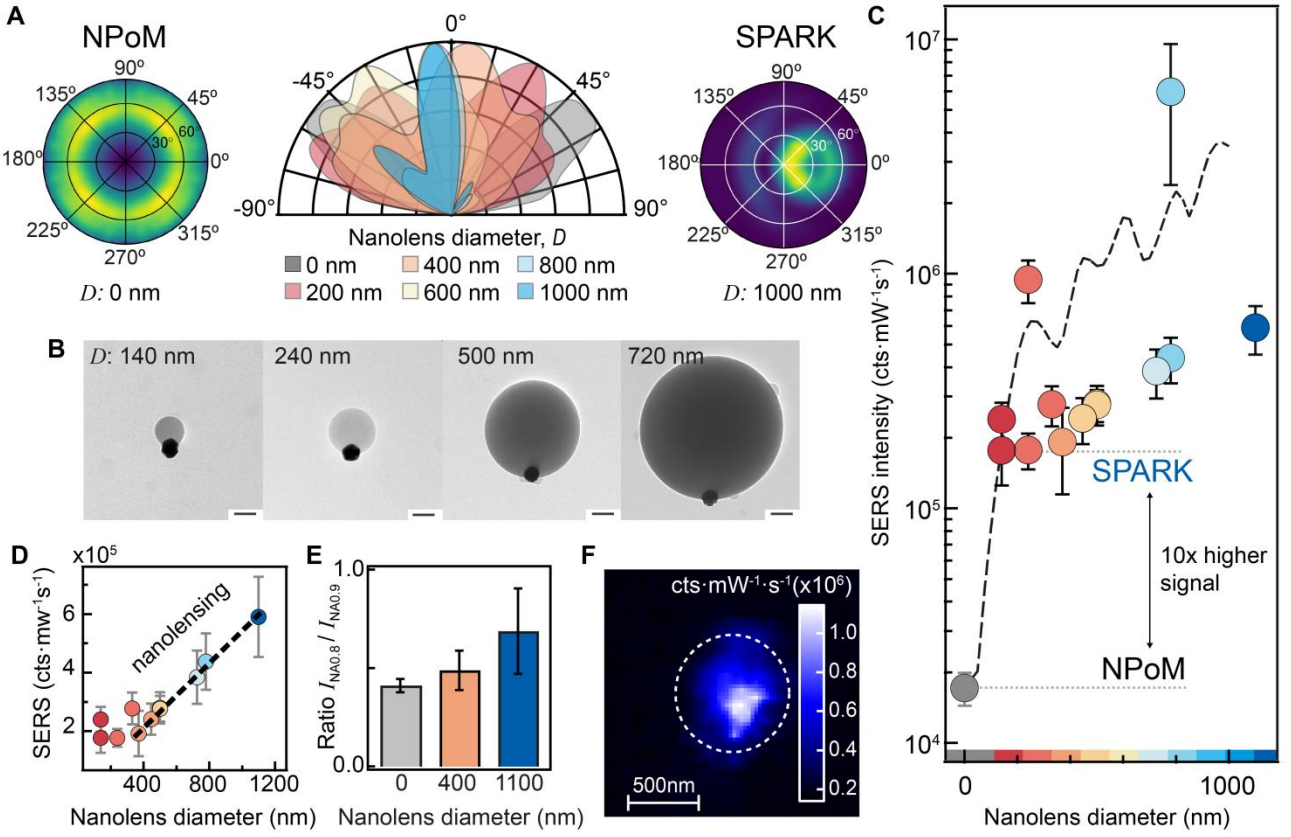

Figure 2 | **Nanolensing effect in the SERS efficiencies of the SPARK geometry.** (**A**) FDTD simulations showing emission angle of a gap-positioned dipole emitter, emitting at 703 nm for different nanolens diameters (D) shown in the vertical plane (centre) and azimuthal plane (left NPoM, right SPARK D = 1000 nm). (**B**) TEM micrographs of SPARKs of increasing nanolens diameter D, scalebars 100 nm. **C,D**) Averaged SERS intensities for SPARKs of different nanolens diameter [log-scale (C), linear-scale (D), >20 different spectra averaged per sample, two samples consistently yielded unusually high SERS intensities]. Dashed line denotes predicted SERS intensities for SPARKs based on enhancement factors from FDTD simulations (SI Appendix §1c). (**E**) High-angle ratio of SERS intensities measured with NA = 0.8 and NA = 0.9 100x objective lenses as a function of nanolens D. (**F**) SERS 2D map scan over a SPARK (analyte: biphenylthiol (BPT), D = 780 nm SPARK, λ_{ex} = 633 nm, 1 s integration time, 40 μW), color scale gives SERS intensity of 1585 cm^{-1} peak, showing localization of SERS signal within SPARK (dashed diameter from dark field image).

RESULTS AND DISCUSSION

SPARKs yield extremely high SERS efficiencies

The base non-hybrid SERS nanostructure used here is Nanoparticle-on-Mirror (NPoM), which already delivers the highest optical confinement inside individual sub-2nm nanogaps (21, 22). This well-established geometry

(Figure 1A: top) is a versatile plasmonic construct consisting of gold nanoparticles (AuNPs) deposited onto a mirror of gold (though other coinage metals also work well). A self-assembled monolayer (SAM) of analytes on the mirror surface precisely controls the size of the nanogaps and ensures that analytes are positioned at the centre of the hot-spots. Spacer layers are not limited to SAMs, but can also consist of 2D materials (23, 24), lipids (25), and rigid molecular scaffolding (26, 27). This geometry facilitates the probing of billions of optically accessible nanojunctions with near identical nanogaps (17, 24–31). The AuNP optically couples to its image charge below the metal surface, forming a virtual plasmonic dimer upon excitation. High angle irradiation induces a coupled vertical dipole with field enhancements approaching 3 orders of magnitude, enabling ultrasensitive and single molecule Raman sensing (17, 31–34). However, the optimal excitation and emission of this coupled mode is at 60° from normal (35), hampering efficient in/outcoupling. Integrating near-field refraction into the geometry is thus extremely advantageous. In addition, incorporating an organosilica lens overcomes the shape influence of gold nanoparticles, which always settle with their flat facets face-down onto the mirror (36). These relatively large facets (>20% of the NP diameter) spread out the confined field distribution (30, 37, 38) and lower the maximum field enhancement that can be attained. Incorporating the AuNPs into an organosilica nanosphere prevents reorientation, fixing the point of initial contact, and as a result the faceting now aids formation of down-facing sharp tips and edges that further enhance the optical field (Figure 1A: bottom).

Experimentally, this dielectric/metallic hybrid nano-architecture is realized by synthesizing an organosilica nanosphere onto AuNPs via a nucleation and growth mechanism using a silane coupling agent, 3-methacryloxypropyltrimethoxysilane (MPTMS) with >90% yield. The MPTMS wetting angle is controlled to be around 50° relative to the AuNP's surface using an amphiphilic polymer (see Figure 1A and SI Appendix Fig. S1). The organosilica nanosphere typically has a size polydispersity (*p. d.*) between 3-10% (SI Appendix Fig. S2A) and a refractive index of $n = 1.50 \pm 0.01$ (SI Appendix Fig. S2B, compared to 1.45 for typical amorphous silica). The resulting dielectric/metallic hybrid colloids (Figure 1B) are deposited onto a gold mirror, forming the geometry depicted in Figure 1A (bottom), henceforth referred to as *Super-efficient Plasmonic nanoArchitectures for Raman Kinetics* (SPARKs).

To characterise how the sub-micron spheres affect the optical in/outcoupling of this geometry, Finite-Difference Time-Domain (FDTD) simulations are employed. A broadband dipole emitter (SI Appendix Fig. S3) is placed midway between a spherical AuNP and the Au mirror surface and the light emission is modelled over 100 fs, both with and without a nanosphere (see supplementary materials: movies V1-V6). At *t*.=.15 fs, it is clear how the $D = 1000$ nm nanosphere drastically redirects outcoupling away from the surface (Figs. 1C and S4-S6), refracting the far-field emission pattern towards the surface normal. The silica spheres are too small to sustain whispering gallery modes, and instead lossy modes are observed. Similar results are found for a dipole emitting at a single wavelength of 703 nm (SI Appendix Fig. S7 and Movies V7,V8). We term this combination of refraction and leaky surface modes, "nanolensing" (submicron spheres being too small to act as a conventional lens for 633 nm light). Full finite element frequency domain calculations on facetted (dodecahedral) AuNPs yield similar results, and reveal that the embedding depth of the AuNP into the nanolens is also important: as the embedding depth increases from 10% to 70%, the light collection increases by two orders of magnitude for even small 100 nm nanolenses (SI Appendix Fig. S8).

The SPARK nano-architectures experimentally yield SERS peak amplitudes exceeding $\sim 10^5$ counts $mW^{-1}\ s^{-1}$ (Figure 1D). Even small $D = 150$ nm opto-plasmonic SPARKs yield average optical efficiencies more than an order of magnitude higher than the already powerful conventional NPoM geometry. Larger 780 nm nanolens sizes further raise this efficiency, yielding up to nearly a hundred-fold higher intensity of a typical NPoM construct. SERS efficiencies up to 10^7 counts $mW^{-1}\ s^{-1}$ are reached for $D = 1100$ nm with an experimental setup optimized for SERS collection (SI Appendix Fig. S10).

Effect of the nanolens on SERS efficiencies

The FDTD simulations show that with increasing nanolens size, the emission angle of the coupled mode for 703 nm light (which is the Stokes wavelength of 1585 cm^{-1} vibrations from the 633 nm pump) can be redirected from 60° (Figure 2A, grey) to near normal emission (Figure 2A, blue), focussing incident light into and collimating emission out of the hot-spot.

Experimentally, the nanolens diameter is controllably grown between $D = 150 \pm 2$ nm (p.d. 7%) and $D = 1100 \pm 9$ nm (p.d. 2%) simply by varying the amount of MPTMS (Figure 2B). Experimental SERS efficiencies are compared for SPARK diameters ranging from $D = 150$ nm to 1100 nm in Figure 2C,D. Note that for SPARKS with a nanolens diameter larger than the diffraction limit, a three-dimensional optimization step was carried out to locate the position with the highest SERS outcoupling on the SPARK geometry. A clear non-lensing contribution is observed as an immediate 10x gain in signal even for a $D = 150$ nm nanolens. This can have

several different contributors, including symmetry breaking and nanoparticle reorientation. The nanolensing and resonant whispering gallery mode contributions to the SERS efficiency give a linear increase with nanolens size starting from $D > 390$ nm (Figure 2D). These experimental results agree well with the predicted intensities from FDTD simulations (dashed line), which show a sharp increase in SERS intensity compared to NPoMs for small nanolenses and a further gradual increase with nanolens size. Quantitative discrepancies likely arise from locating the dipole emitter in the FDTD simulations only at the central position inside the gap.

Nanolensing is further corroborated experimentally by quantifying the high-angle collection sensitivity, comparing total SERS collected with objectives of NA = 0.8 *vs* 0.9 (Figure 2E). This ratio quantifies the fraction of high-angle emission (53° *vs* 64°) and as the nanolens size is increased, the ratio becomes closer to one, showing that the emission is indeed angled closer to the normal. Reciprocally, this also implies that incoupling of light is more tightly focussed onto the AuNP, which indeed is observed in 2D real-space SERS mapping of a $D = 780$ nm SPARK (Figure 2F), where even sub-λ translations of 50 nm drastically affect the measured SERS intensity as expected from tight sub-diffraction-limited lensing.

To accurately estimate the SERS enhancements reached with these SPARK nano-architectures and compare with other systems, the number of molecules probed in the hotspot must be determined. The Janus hybrid changes the contact between the AuNP and mirror from a flat facet to a protruding tip/edge by geometrical constraints, as visible in SEM images (Figure 3A, SI Appendix Fig. S11). Therefore, a more strongly confined electromagnetic field is expected than for the NPoM. Earlier studies on nanogap conductance using biphenylthiol (BPT) found ~200 molecules in the active plasmonic volume (39). The geometry of a typical AuNP (icosahedron) suggests that the tip supports a 9-fold reduced area compared to the flat facet area from SEM micrographs (see SI Appendix Fig. S12), hence only 22 ± 7 molecules are probed in the SPARK geometry. This in turn implies that the SERS signals of SPARKs stem from ~10x fewer molecules than in the bare NPoMs, resulting in $8 \cdot 10^3$ to $3 \cdot 10^4$ cts mW^{-1} s^{-1} molecule^{-1} for $D = 150$ nm - 1100 nm. With an optimized setup, intensities of $5 \cdot 10^5$ cts mW^{-1} s^{-1} molecule^{-1} are reached. These measured SERS efficiencies are the highest reported to date (Table T1). Comparing against the Raman signal of an analyte solution, we experimentally determine enhancement factors of $4 \cdot 10^8$ for NPoMs increasing to 10^{11} for SPARKs (see calculations in SI Appendix §5 and Fig. S13).

High signal-to-noise ratios: Detecting isotopologues

The extreme SERS efficiencies from SPARKs open up avenues to a wide range of applications. Firstly, molecular properties that were previously inaccessible can now be probed. Isotopologues are molecules in which at least one constituent atom carries an extra neutron. Artificially synthesized isotopologues have been used for sensing applications as an internal standard (40–42) and to distinguish between few-molecule and single-molecule SERS (SM-SERS) (43, 44). Naturally abundant isotopologues have only been detected in SM-SERS (45, 46), since the isotopologue peak is washed out in average spectrum (45). The exceptional SERS signal-to-noise ratios (>10^3 : 1 for a 250 μJ laser dose) in our nano-architectures allow detection of ^{13}C isotopologues in the average spectra of non-resonant molecules at natural abundance (Figure 3B). This is the first time that naturally abundant isotopologues are directly measured in an ensemble of molecules. We use 4'-mercaptobiphenylcarbonitrile (BPT-CN), which has the same structure as BPT but with a cyano group added (18). By natural abundance, the carbon atom located in the cyano triple bond is a ^{13}C atom in 1.1% of the molecules. DFT calculations predict that the vibrational frequency for the C≡N stretch mode is shifted by -52 cm^{-1} in the BPT-^{13}CN, down to 2154 ± 1 cm^{-1} from 2206 ± 1 cm^{-1} (SI Appendix §6). In the SPARK geometry, this C≡N stretching peak is indeed detected above both background and noise in accumulated spectra taken at laser powers < 5 μW (Figure 3B, insets).

The ability to detect this isotope peak enables us to quantify the number of molecules contributing to the SERS signal in the SPARKs. SERS spectra are collected from 36 individual SPARKs, and the percentage of ^{13}C≡N signal is obtained from the maxima of Gaussians fitted to the ^{13}C≡N and ^{12}C≡N peaks. The histogram of occurrences does not show a clear peak at f=1.1% but rather displays both lower and higher signal intensities, suggesting fewer than ~100 molecules probed. We numerically model the nanogap using a hexagonal array of points with a lattice spacing of 0.58 nm representing the analyte layer (based on the known spacing of molecules in a biphenyl thiol SAM (47)), and a rotationally symmetric approximation for the electric field distribution in the nanogap (SI Appendix Fig. S14). Each molecule is assigned a 0.011 probability to represent a ^{13}C isotopologue. For each facet size, 2000 different realisations of the nanogap are simulated, extracting the ^{13}C≡N : ^{12}C≡N SERS intensity ratio for each instance. This yields a histogram of the occurrence frequency of each intensity ratio, for different facet sizes. Comparing the results of this model to the experimental data (Figure 3C), the best fit is

found for a facet diameter 10 nm, which agrees reasonably with pentagonal facet size estimates from electron micrographs (8 nm). This supports the notion that the colloidal nanolens orients the AuNP's vertex downwards onto the mirror, contributing to the high SERS efficiencies for even small 150 nm SPARKs by way of higher field confinement.

To highlight the versatility of SPARKs and show that such enhanced signals are not unique to BPT or BPT-CN, a range of different analytes are explored including 4-mercaptobenzoic acid (4-MBA) (48), trans-1,2-bis(4-pyridyl)ethylene (B4PE) (49, 50) and benzenethiol. All these analytes show similar high SERS efficiencies in SPARK geometries (SI Appendix Fig. S15). Rhodamine 6G (R6G) requires laser powers to be below 3 μW for consistent SERS sensing, since R6G is electronically-resonant and degrades at even these low laser powers due to the more efficient incoupling of light into the SPARK nanostructure.

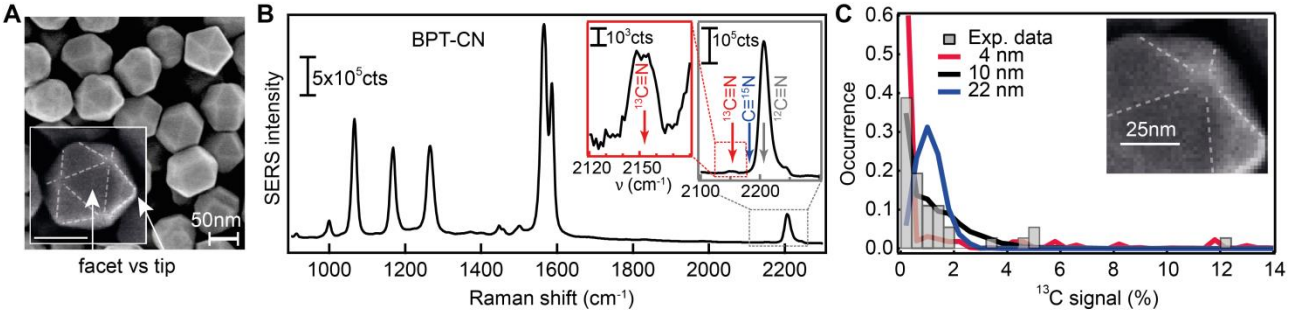

Figure 3 | **Using the SPARK geometry to detect isotopologues.** (**A**) SEM micrograph of AuNPs. (**B**) SERS spectrum for BPT-CN, obtained with D = 1100 nm SPARK. Fifty spectra of 1 s integration time were accumulated at low laser power (5 μW) to avoid any molecular damage or gold atom movements. Insets expand peak from ^{13}C≡N bond. **(C)** Experimental histogram for the occurrence (fraction) of SERS peaks from ^{13}C≡N bonds (grey), and numerically calculated ^{13}C≡N SERS intensity percentages for different nanotip diameters (colored). Insets in (A,C) show facets outlined (dashed lines) and the AuNP nanotips.

Fast sensing: Probing molecular dynamics at 17 μs acquisition times

The discovery and development of SERS has brought Raman sensing acquisition times down from seconds to milliseconds (18, 34, 51, 52). The greatly increased signals achieved by SPARK nano-architectures can now facilitate the collection of SERS spectra at sub-millisecond integration times, to observe the dynamic behaviour of molecules at surfaces in more detail. SERS spectra are collected at 10 μs integration times with only 7 μs dead time (Figure 4). This unlocks the study of previously inaccessible fast dynamics via real-time monitoring. For example, by pumping plasmonic hotspots with enough laser light, single atom protrusions or *pico-cavities* can be induced that further localize the field down to sub-1nm^3 optical mode volumes (17) (see SI Appendix Fig. S16). Pico-cavities provide an additional several-hundred-fold enhancement facilitating single molecule detection (17, 18). The SPARK system thus allows analysis of the formation dynamics of single atom protrusions in real-time as Au atoms are pulled out from the gold crystal lattice (Figure 4A:top). The formation of the pico-cavity is recognised by the appearance of a set of new Raman lines from the closest bonds (Figure 4A:middle). Tracking the rise of these lines over time reveals that such a single atom protrusion is formed over 60 ± 5 μs (at 95% total signal change), in a gradually evolving appearance. Previous studies of adatom movement via electron microscopy or scanning probe microscopy were unable to resolve such timescales, which for this adatom process are seen to be surprisingly slow with atom velocities of ~2 μm s^{-1}. Although the metal adatom movement is found to be light-activated (with 0.8 eV activation energy as expected for adatoms on Au) (17), the high-speed observations here do not correspond to a model of thermal activation over a single barrier of this height.

A second phenomenon observed is the fleeting reconstruction of nano-scale patches on the gold facet surfaces inside the plasmonic hot-spot, which are seen as brief local increases in the background SERS signal from free electrons in the metal, which we recently reported (53) and are referred to here as *flares*. Even previous high speed SERS measurements (with 10 ms acquisition times) (18, 34, 53) have averaged over such dynamics, but these can now be clearly resolved (Figure 4B). Averaging the signal between 400-1200 cm^{-1} allows us to fit a flare rise time of 70 ± 5 μs with a similar decay time. The flare timespan of 200 μs is not yet understood, and again is much longer than acoustic or thermal timescales in metal nanoparticles. The dynamics after the flare switches off show a brief dip before recovering to a background intensity reduced by a third of that before the flare. This suggests we observe relaxation in the gold crystal lattice as a result of the local surface

reconstruction. To ensure that these rise times are not a result of instrument limitations, faster feature changes were identified as well (SI Appendix Fig. S16).

Combining the enhancement from the pico-cavity with the enhancement from the SPARKs provides sufficient signal to track the motion of single molecules with 17 μs time resolution (Figure 4C:top). Under illumination with just enough laser light to induce chemical processes, changes in the peak position are seen, which indicate the molecule is deforming (Figure S14D). Even rapid changes in the vibrational configuration (marked by arrows) are captured (Figure 4C:bottom), demonstrating how such fast molecular dynamics can now fully be tracked in real-time using SERS, in addition to the atomic dynamics on metal surfaces.

On account of the ultrafast nature of the Raman emission process and the picosecond relaxation times of the resulting vibrations (54), saturation does not occur as for fluorescence. Thus, in such a highly optimised SERS substrate, a single non-resonant molecule can be excited far more frequently than a dye or quantum dot. As a result, our nano-architecture is able to generate higher photon count rates than conventional single photon light sources. Integrating the single molecule signal for a single peak yields integrated count rates between $0.6 \cdot 10^5$ - $8 \cdot 10^6$ cts s^{-1} (SI Appendix Fig. S17), exceeding nearly all single dye molecule and quantum dot count rates reported to date (SI Appendix Table T2) (19, 20, 55–63). Single molecule SERS in such an optimised geometry is thus a powerful candidate for single photon light sources with superior count rates without suffering from blinking or bleaching. Nevertheless, for such devices to be realistically viable, single atom protrusions will need to be chemically- or optically-stabilized (17, 18) indefinitely and the single molecule devices will have to be protected against degradation.

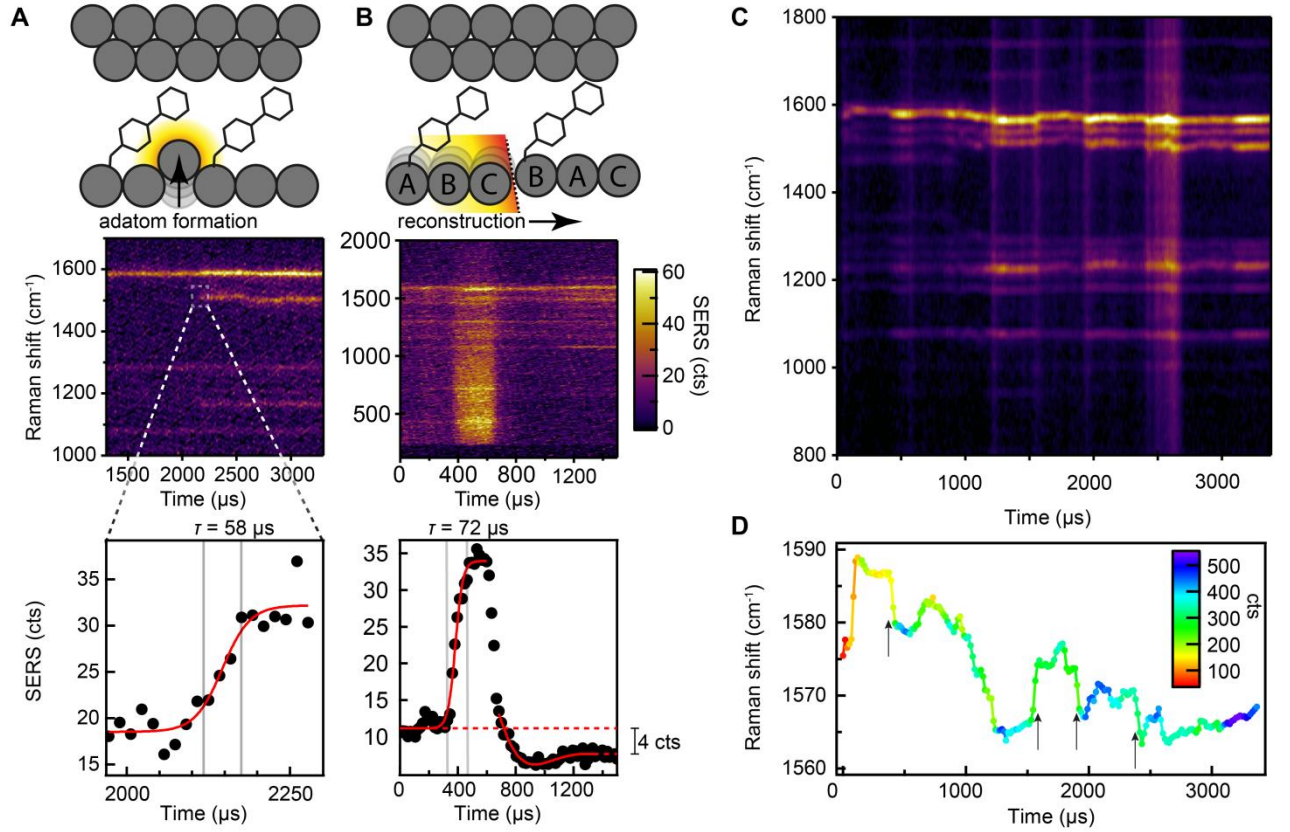

Figure 4 | **Ultrafast SERS acquisitions with 10 μs integration times** (7 μs between spectra) of BPT in a D = 150 nm SPARK geometry from 35 μW laser power using an EMCCD with 50x gain. (**A**) The formation of a pico-cavity (single Au atom protrusion) tracked in real-time. (**a**: top) Scheme depicting atom pull-out, (**A**: middle) SERS time scan showing the appearance of new lines at 1510 cm^{-1} and 1170 cm^{-1} indicating formation of pico-cavity, (**A**: bottom) SERS intensity during pico-cavity formation: measured rise-time τ is 60 ± 5 μs (at 95% signal change). (**B**) The formation and destruction of a *flare* tracked in real time. (**B**: top) Scheme depicting proposed mechanism of flare event (reconstruction of gold lattice). (**B**: middle) SERS time scan showing the rise and fall in SERS background. (**B**: bottom) averaged SERS background showing rise and fall time of flare ~70 ± 5 μs. (**C**) SERS pico-cavity time scan over 3.4 ms showing the conformational changes of a single molecule with 17 μs time resolution. (**D**) Peak positions of bond in pico-cavity *vs* time, from (**C**), showing that each conformation change is captured by multiple frames even if rapid.

CONCLUSIONS

Several factors aid in the utility of the SPARKs. The high refractive index of the organosilica nanolenses as well as their smooth surfaces (Figure 2A) are beneficial to the nanolensing effect. The sub-micron-size sphere is lossy, allowing the out-coupled light to radiate rather than being trapped in whispering gallery modes inside the sphere. The partial embedding of AuNPs by ~50% of their diameter into the silica sphere injects the SERS signal directly into the nanolens, without external reflection at the silica/air interface. With the AuNP further outside the nanolens, optical emission reflects from the sphere surface into high angle directions where it cannot be collected, precluding simple nanoparticle attachment of dielectric spheres to AuNPs. Compared to the 360° torus emitted from nanoparticle dimer, the SPARK emission pattern is still more favourable (63). Interestingly, including a mirror (64, 65) and even a Fabry-Pérot cavity (11) still does not reach the $> 5 \cdot 10^5$ single molecule counts^{-1} mW^{-1} s^{-1} molecule^{-1} SERS efficiencies observed here.

In summary, these SPARK nano-constructs embody a versatile sensing platform, which achieves high SERS collection efficiencies produced by a combination of refractive and plasmonic optics. Experimental characterisation and full wave simulations show that the incoupling and outcoupling of laser-driven SERS signals from molecules assembled inside the integrated nanogaps is enhanced through the combined effects of nanolensing, re-excitation and symmetry breaking as well as light-concentration through nanoscale reorientation of the AuNP. The measured SERS efficiencies (10^7 cts mW^{-1} s^{-1} and 10^6 cts mW^{-1} s^{-1} molecule^{-1}) are the highest reported to date. Our results expose new avenues to detect trace amounts of analyte molecules, and even naturally abundant isotopes. We show that the extreme efficiencies provided by SPARKs allow us to perform single-molecule SERS at microsecond integration times, which is of immense value for studying dynamics of materials reconstructions, chemical reactions and photocatalysis. We demonstrated detection of gold lattice reconstruction and the formation of single atom protrusions (*pico-cavities*) in real-time. With count rates of $5 \cdot 10^5$ to $3 \cdot 10^7$ s^{-1} molecule^{-1}, we showed non-resonant molecules become even brighter than single molecule dyes (19). Combining this with the improved excitation efficiencies opens up possibilities of using single non-resonant molecules as widespread optical devices.

MATERIALS AND METHODS

Materials

Gold spheres (diameter 80 nm) stabilized in citrate buffer are purchased from Sigma Aldrich and used as received. Ammonia solution (35 wt.%) is obtained from Fisher Scientific. The following chemicals are purchased from Aldrich: (3-mercaptopropyl)trimethoxysilane (MPTMS, 98%) and 2,2′-azobis(2-methylpropionitrile) (AIBN, 98%). All water is deionized with a Millipore Synergy UV water purification system and has a resistivity of 18.2 MΩ cm. Anhydrous ethanol (Sigma-Aldrich, < 0.003% H_2O) is used to prepare self-assembled monolayers (SAMs) of analytes. Analytes used are: biphenyl-4-thiol (BPT, Sigma-Aldrich, 97%), 4′-mercaptobiphenylcarbonitrile (BPT-CN, 97%), thiophenol (97%, Merck), 1,2-bis(2-pyridyl)ethylene (97%, Sigma Aldrich), 4-mercaptobenzoic acid (97%, Sigma Aldrich) and rhodamine 6G (95%, Sigma Aldrich). PNIPAM-SH (15k) is prepared according to ref. (66).

Gold-organosilica hetero-dimer synthesis

Metallic/dielectric hybrid hetero-dimers are prepared by using gold nanoparticles (AuNPs) as seeds for nucleation and growth. Our approach is a version of the reactions presented in refs. (67–69), modified to accommodate AuNPs as seeds. In a typical synthesis, 2 mL of an aqueous solution of PNIPAM-SH (1 g/L) is added to 5 mL of AuNPs. After stirring for 2 h to allow the PNIPAM-SH to adhere to the AuNP surface, excess PNIPAM-SH is washed away by centrifuging the particles three times at 4000 g, each time replacing the supernatant with 12 mL H_2O. By the final centrifugation step, the volume of the dispersion is reduced to 0.3 mL. To grow MPTMS droplets onto the AuNPs, 1 µL ammonia and a chosen amount of MPTMS are added to the dispersion. The reaction mixture is stirred for 2 h at 100 rpm, during which time nucleation and condensation of the MPTMS onto the AuNPs occurs. Subsequently, 2 mg of AIBN is added to the reaction mixture, after which it is placed in a water bath thermostated at 70 °C. This heating step cross-links the methacrylate groups in the MPTMS lobes, creating solid particles. After 2-3 h of cross-linking, the reaction is quenched by adding ethanol and the particles are washed by centrifugation in Eppendorf tubes (3000 rpm). The washing step is repeated at least three times to remove reactants and secondary nuclei. The particles must be stored in ethanol, as hydroxide ions in water etch the MPTMS lobe over time. Note also that PNIPAM-SH adsorption to gold is time-dependent; longer (>12 h) PNIPAM-SH coating of the AuNPs results in fully encapsulated particles. Organosilica sphere sizes as a function of

MPTMS concentration are shown in SI Appendix Fig. S2. For example, 3 µL MPTMS results in D~0.5 µm organosilica lobes.

'SPARK' sample preparation

Samples for SERS measurement (*Superefficient Plasmonic nanoArchitectures for Raman Kinetics*, SPARKs) are prepared by depositing gold-organosilica hetero-dimers onto template-stripped gold (TSG) mirrors decorated with a self-assembled monolayer (SAM) of analyte. TSG mirrors are prepared as described in ref.(70) Biphenyl-4-thiol (BPT) is directly dissolved in ethanol to make a 1 mM solution. Pieces of TSG are placed in 2-3 mL of this solution and left to form a SAM over two days. The gold mirrors are then rinsed with ethanol and dried with nitrogen. Gold-organosilica hetero-dimers are then deposited from ethanol by placing 60-100 µL of dispersion onto a piece of TSG with a SAM. After 10 min, the sample is rinsed with ethanol and dried with N_2. For control samples, gold nanospheres are deposited by placing 40-60 µL of dispersion in citrate buffer onto a TSG plate with a SAM. After 20-30 s, excess particles are rinsed off with water and the samples dried with N_2. The deposition time required to reach acceptable surface coverage is longer for SPARKs than for AuNPs, most likely related to a difference in surface charge of organosilica compared to AuNPs.

SERS measurements

Combined SERS and scattering experiments are performed using a modified Olympus BX51 microscope in reflective dark field geometry. The samples are illumined with a focused white light source (100 W halogen lamp, angle of incidence of 60°). The dark-field scattered light is analyzed after collection with a fiber-coupled Ocean Optics QE65000 cooled spectrometer. SERS spectra are recorded on a homebuilt Raman spectrometer coupled into the microscope. A spectrally filtered 632.8 nm helium-neon laser is used as the excitation source. The elastically scattered laser light is filtered with two Semrock 633 nm StopLine® single-notch filters. The signal is coupled into an Andor Shamrock i303 spectrograph and Newton EMCCD.

A tightly focussed laser spot, near the diffraction limit, is essential for the NPoM geometry, which requires high NA in-coupling. For focussing and collection, three different types of 100x microscope objectives are used. To calculate enhancement factors, an Olympus 0.8 NA objective with long working distance is used, since the long working distance allows for Raman measurements to be taken from solutions of analytes and compared with SERS from the SPARK substrates. Unless stated otherwise, this 0.8 NA long working distance Olympus objective is used for focussing and collection of SERS spectra. To compare the SERS intensities for different NAs (Figure 2E), an Olympus 0.9 NA and a long working distance Olympus 0.8 NA objective are used. Finally, for obtaining SERS spectra with optimised counts, a Zeiss 0.9 NA objective is used.

For SPARKs with a nanolens larger than the diffraction limit (i.e. nanolens >300nm) a three dimensional optimisation step is performed before acquiring spectra, to locate the position where light is optimally coupled into and out of the nanostructure. For SPARKs with a sub-diffraction limited nanolens (i.e. nanolens <300nm), no optimisation is necessary other than centering the particle in the laser spot.

Fast SERS measurements

For the fast kinetic measurements, an Andor EMCCD is used with 50x EM gain and a 4.9 µs shift speed. The sample is irradiated with 35 µW laser power. The SERS signal is focussed onto a single line on the top of the CCD array and imaged using a 'fast kinetics mode' where the image is sequentially shifted down the CCD providing 200 spectra in 3.4 ms. The integration time is set to 10 µs and the read time is 7 µs, resulting in a 17 µs cycle time between spectra.

FDTD simulations

The optical response and far-field emission of the NPoM and SPARK structures are obtained by performing 3D full-wave finite-difference time-domain (FDTD) simulations using commercial software, Lumerical FDTD version 8.18.1298. The molecular spacer is modelled as a 1.2 nm thick dielectric material with a refractive index 1.45, and the nanolens (diameter 0 – 1000 nm) is modelled as a dielectric sphere with refractive index 1.50. The AuNP is modelled as a sphere with a diameter 80 nm which is 50% embedded inside the nanolens. The gold permittivity is taken from Johnson and Christy (71). The simulation domain size is 10 µm × 10 µm × 1.6 µm. We utilize the conformal meshing scheme between dielectric interfaces, but not on metal interfaces, with a maximum step size of 100 nm in all directions. Small mesh refinements of 20 nm, 4 nm and 0.06 nm are used around the nanolens, AuNP and spacer, respectively. The nanolensing effect on SERS signals is evaluated in two parts: excitation and emission. For excitation, the structure is excited by a broadband horizontally-polarized

Gaussian beam with NA = 0.8 which is laterally offset by 100 nm from the centre of the AuNP (though other offsets are also tested). For emission, a broadband electric dipole emitter is placed at the middle of the spacer directly below the AuNP. The far-field emission profile is calculated from the recorded fields on a 10 μm × 10 μm monitor located 1.2 μm above the substrate.

COMSOL simulations

Numerical scattering calculations on spatially-resolved dodecahedral AuNPs with facet-down configurations are performed using the commercial finite element solver COMSOL Multiphysics Version 5.3a with RF module. The material and geometrical parameters are identical to those used for FDTD simulations above. Angle-resolved far field Raman scattering is approximated via two successive simulations. First, the NPoM or SPARK system is excited by a background Gaussian beam of 633nm laser wavelength and microscope numerical aperture of NA = 0.8. To accommodate for the strong focussing of the beam we approximate it using a plane wave expansion, i.e. a rigorous solution of Maxwell's equations in vacuum, instead of a paraxial representation. The second calculation assumes an excited Raman active BPT molecule in the plasmonic hotspot with isotropic polarizability. This assumption does not strongly influence the results since the plasmonic fields in the nanogap are predominantly z-polarized and thus aligned with the BPT molecules. We use a dipole source of 680 nm wavelength and of current strength proportional to the field at the hotspot to classically emulate the non-linear quantum mechanical scattering process. Angle-resolved far field power density flow is extracted using the methodology from ref. (72).

Data Availability Statement. All relevant data present in this publication can be accessed at https://www.repository.cam.ac.uk/[intentional blank]. The source data underlying Figs. 1–4 are provided.

Acknowledgements:

MK is grateful to the European Commission for a Marie Curie fellowship (grant 7020005, SPARCLEs) and to Peterhouse for a Research Associateship. BdN acknowledges financial support from the Leverhulme Trust through an Early Career Fellowship and from the Newton Trust through matching funding, and thanks Hughes Hall for a fellowship. MK and BdN are also grateful for a Pump Prime grant from the Winton Programme for the Physics of Sustainability. RC acknowledges support from Trinity College, University of Cambridge. SJB thanks the European Commission for a Marie Curie fellowship (grant 658360, NANOSPHERE). OSO acknowledges the support of a Rubicon fellowship from the Netherlands Organisation for Scientific Research. JJB acknowledges support from the Engineering and Physical Sciences Research Council (EPSRC) UK through grants EP/L027151/1, EP/R020965/1, and NanoDTC EP/L015978/1. O.A.S. acknowledges the ERC-2016 Consolidator Grant (CAM-RIG, 726470) and EPSRC Programme Grant (NOtCH, EP/L027151/1) for funding. O.H. also acknowledges support from the EPSRC through grants EP/L024926/1 and EP/L027151/1.

REFERENCES

1. H. Yu, Y. Peng, Y. Yang, Z.-Y. Li, Plasmon-enhanced light–matter interactions and applications. *npj Computational Materials* **5**, 45 (2019).
2. J. A. Schuller, *et al.*, Plasmonics for extreme light concentration and manipulation. *Nature Materials* **9**, 193 (2010).
3. D. A. Iranzo, *et al.*, Probing the ultimate plasmon confinement limits with a van der Waals heterostructure. *Science* **360**, 291–295 (2018).
4. S. Gwo, H.-Y. Chen, M.-H. Lin, L. Sun, X. Li, Nanomanipulation and controlled self-assembly of metal nanoparticles and nanocrystals for plasmonics. *Chem. Soc. Rev.* **45**, 5672–5716 (2016).
5. D. Graham, *et al.*, Theory of SERS enhancement: general discussion. *Faraday Discuss.* **205**, 173–211 (2017).
6. J. Zhang, *et al.*, Whispering-gallery nanocavity plasmon-enhanced Raman spectroscopy. *Scientific Reports* **5**, 15012 (2015).
7. I. Alessandri, Enhancing Raman Scattering without Plasmons: Unprecedented Sensitivity Achieved by TiO2 Shell-Based Resonators. *J. Am. Chem. Soc.* **135**, 5541–5544 (2013).
8. N. Bontempi, I. Vassalini, S. Danesi, I. Alessandri, ZORRO: zirconium oxide resonators for all-in-one Raman and whispering-gallery-mode optical sensing. *Chem. Commun.* **53**, 10382–10385 (2017).
9. N. Bontempi, I. Vassalini, I. Alessandri, All-dielectric core/shell resonators: From plasmon-free SERS to multimodal analysis. *Journal of Raman Spectroscopy* **49**, 943–953 (2018).
10. A. M. Kern, *et al.*, Enhanced single-molecule spectroscopy in highly confined optical fields: from λ/2-Fabry–Pérot resonators to plasmonic nano-antennas. *Chem. Soc. Rev.* **43**, 1263–1286 (2014).

11. Y. Guo, *et al.*, Using a Fabry–Perot Cavity to Augment the Enhancement Factor for Surface-Enhanced Raman Spectroscopy and Tip-Enhanced Raman Spectroscopy. *The Journal of Physical Chemistry C* **122**, 14865–14871 (2018).
12. I. Alessandri, N. Bontempi, L. E. Depero, Colloidal lenses as universal Raman scattering enhancers. *RSC Advances* **4**, 38152–38158 (2014).
13. J. Y. Lee, *et al.*, Near-field focusing and magnification through self-assembled nanoscale spherical lenses. *Nature* **460**, 498 (2009).
14. Y. Yan, *et al.*, Microsphere-Coupled Scanning Laser Confocal Nanoscope for Sub-Diffraction-Limited Imaging at 25 nm Lateral Resolution in the Visible Spectrum. *ACS Nano* **8**, 1809–1816 (2014).
15. H. Zhu, B. Yan, S. Zhou, Z. Wang, L. Wu, Synthesis and super-resolution imaging performance of a refractive-index-controllable microsphere superlens. *J. Mater. Chem. C* **3**, 10907–10915 (2015).
16. B. Hou, *et al.*, Microsphere Assisted Super-resolution Optical Imaging of Plasmonic Interaction between Gold Nanoparticles. *Scientific Reports* **7**, 13789 (2017).
17. F. Benz, *et al.*, Single-molecule optomechanics in "picocavities." *Science* **354**, 726 (2016).
18. C. Carnegie, *et al.*, Room-Temperature Optical Picocavities below 1 nm3 Accessing Single-Atom Geometries. *J. Phys. Chem. Lett.* **9**, 7146–7151 (2018).
19. B. Lounis, W. E. Moerner, Single photons on demand from a single molecule at room temperature. *Nature* **407**, 491 (2000).
20. N. Somaschi, *et al.*, Near-optimal single-photon sources in the solid state. *Nature Photonics* **10**, 340 (2016).
21. J. J. Baumberg, J. Aizpurua, M. H. Mikkelsen, D. R. Smith, Extreme nanophotonics from ultrathin metallic gaps. *Nat. Mater.* **18**, 668–678 (2019).
22. G.-C. Li, Q. Zhang, S. A. Maier, D. Lei, Plasmonic particle-on-film nanocavities: a versatile platform for plasmon-enhanced spectroscopy and photochemistry. *Nanophotonics* **7**, 1865–1889 (2018).
23. J. Mertens, *et al.*, Controlling Subnanometer Gaps in Plasmonic Dimers Using Graphene. *Nano Letters* **13**, 5033–5038 (2013).
24. M.-E. Kleemann, *et al.*, Strong-coupling of WSe2 in ultra-compact plasmonic nanocavities at room temperature. *Nature Communications* **8**, 1296 (2017).
25. R. W. Taylor, *et al.*, Watching individual molecules flex within lipid membranes using SERS. *Scientific Reports* **4**, 5940 (2014).
26. T. Ding, *et al.*, Controllable Tuning Plasmonic Coupling with Nanoscale Oxidation. *ACS Nano* **9**, 6110–6118 (2015).
27. C. Readman, *et al.*, Anomalously Large Spectral Shifts near the Quantum Tunnelling Limit in Plasmonic Rulers with Subatomic Resolution. *Nano Lett.* **19**, 2051–2058 (2019).
28. M. Hu, A. Ghoshal, M. Marquez, P. G. Kik, Single Particle Spectroscopy Study of Metal-Film-Induced Tuning of Silver Nanoparticle Plasmon Resonances†. *Journal of Physical Chemistry C* **114** (2010).
29. C. Lumdee, B. Yun, P. G. Kik, Wide-Band Spectral Control of Au Nanoparticle Plasmon Resonances on a Thermally and Chemically Robust Sensing Platform. *J. Phys. Chem. C* **117**, 19127–19133 (2013).
30. C. Tserkezis, *et al.*, Hybridization of plasmonic antenna and cavity modes: Extreme optics of nanoparticle-on-mirror nanogaps. *Phys. Rev. A* **92**, 053811 (2015).
31. B. de Nijs, *et al.*, Unfolding the contents of sub-nm plasmonic gaps using normalising plasmon resonance spectroscopy. *Faraday Discuss.* **178**, 185–193 (2015).
32. D. O. Sigle, *et al.*, Observing Single Molecules Complexing with Cucurbit[7]uril through Nanogap Surface-Enhanced Raman Spectroscopy. *J. Phys. Chem. Lett.* **7**, 704–710 (2016).
33. R. Chikkaraddy, *et al.*, Single-molecule strong coupling at room temperature in plasmonic nanocavities. *Nature* **535**, 127 (2016).
34. B. de Nijs, *et al.*, Plasmonic tunnel junctions for single-molecule redox chemistry. *Nature Communications* **8**, 994 (2017).
35. R. Chikkaraddy, *et al.*, How Ultranarrow Gap Symmetries Control Plasmonic Nanocavity Modes: From Cubes to Spheres in the Nanoparticle-on-Mirror. *ACS Photonics* **4**, 469–475 (2017).
36. D. O. Sigle, *et al.*, Monitoring Morphological Changes in 2D Monolayer Semiconductors Using Atom-Thick Plasmonic Nanocavities. *ACS Nano* **9**, 825–830 (2015).
37. N. Kongsuwan, A. Demetriadou, R. Chikkaraddy, J. J. Baumberg, O. Hess, Fluorescence enhancement and strong-coupling in faceted plasmonic nanocavities. *EPJ Appl. Metamat.* **5** (2018).
38. Y. Huang, L. Ma, J. Li, Z. Zhang, Nanoparticle-on-mirror cavity modes for huge and/or tunable plasmonic field enhancement. *Nanotechnology* **28**, 105203 (2017).
39. F. Benz, *et al.*, Generalized circuit model for coupled plasmonic systems. *Opt. Express* **23**, 33255–33269 (2015).
40. R. Goodacre, D. Graham, K. Faulds, Recent developments in quantitative SERS: Moving towards absolute quantification. *TrAC Trends in Analytical Chemistry* **102**, 359–368 (2018).
41. A. Subaihi, *et al.*, Quantitative detection of codeine in human plasma using surface-enhanced Raman scattering via adaptation of the isotopic labelling principle. *Analyst* **142**, 1099–1105 (2017).

42. A. Subaihi, *et al.*, Towards improved quantitative analysis using surface-enhanced Raman scattering incorporating internal isotope labelling. *Anal. Methods* **9**, 6636–6644 (2017).
43. J. A. Dieringer, R. B. Lettan, K. A. Scheidt, R. P. Van Duyne, A Frequency Domain Existence Proof of Single-Molecule Surface-Enhanced Raman Spectroscopy. *J. Am. Chem. Soc.* **129**, 16249–16256 (2007).
44. A. B. Zrimsek, N. L. Wong, R. P. Van Duyne, Single Molecule Surface-Enhanced Raman Spectroscopy: A Critical Analysis of the Bianalyte versus Isotopologue Proof. *J. Phys. Chem. C* **120**, 5133–5142 (2016).
45. P. G. Etchegoin, E. C. Le Ru, M. Meyer, Evidence of Natural Isotopic Distribution from Single-Molecule SERS. *J. Am. Chem. Soc.* **131**, 2713–2716 (2009).
46. C. G. Artur, R. Miller, M. Meyer, E. C. L. Ru, P. G. Etchegoin, Single-molecule SERS detection of C60. *Phys. Chem. Chem. Phys.* **14**, 3219–3225 (2012).
47. D. G. Matei, H. Muzik, A. Gölzhäuser, A. Turchanin, Structural Investigation of 1,1′-Biphenyl-4-thiol Self-Assembled Monolayers on Au(111) by Scanning Tunneling Microscopy and Low-Energy Electron Diffraction. Langmuir 28, 13905-13911 (2012).
48. A. Michota, J. Bukowska, Surface-enhanced Raman scattering (SERS) of 4-mercaptobenzoic acid on silver and gold substrates. *Journal of Raman Spectroscopy* **34**, 21–25 (2003).
49. W. Yang, J. Hulteen, G. C. Schatz, R. P. Van Duyne, A surface-enhanced hyper-Raman and surface-enhanced Raman scattering study of trans-1,2-bis(4-pyridyl)ethylene adsorbed onto silver film over nanosphere electrodes. Vibrational assignments: Experiment and theory. *J. Chem. Phys.* **104**, 4313–4323 (1996).
50. E. A. Sprague-Klein, *et al.*, Photoinduced Plasmon-Driven Chemistry in trans-1,2-Bis(4-pyridyl)ethylene Gold Nanosphere Oligomers. *J. Am. Chem. Soc.* **140**, 10583–10592 (2018).
51. C. Zong, C.-J. Chen, M. Zhang, D.-Y. Wu, B. Ren, Transient Electrochemical Surface-Enhanced Raman Spectroscopy: A Millisecond Time-Resolved Study of an Electrochemical Redox Process. *Journal of the American Chemical Society* **137**, 11768–11774 (2015).
52. A. J. Wain, M. A. O'Connell, Advances in surface-enhanced vibrational spectroscopy at electrochemical interfaces. *Advances in Physics: X* **2**, 188–209 (2017).
53. C. Carnegie, *et al.*, Flickering nm-scale disorder in a crystal lattice tracked by plasmonic 'flare' light emission. *Nature Communications* **11**, 682 (2020).
54. N.-H. Seong, Y. Fang, D. D. Dlott, Vibrational Energy Dynamics of Normal and Deuterated Liquid Benzene. *Journal of Physical Chemistry A* **113**, 1445–1452 (2009).
55. S. Strauf, *et al.*, High-frequency single-photon source with polarization control. *Nature Photonics* **1**, 704 (2007).
56. A. Renn, J. Seelig, V. Sandoghdar, Oxygen-dependent photochemistry of fluorescent dyes studied at the single molecule level. *Molecular Physics* **104**, 409–414 (2007).
57. G. Wrigge, I. Gerhardt, J. Hwang, G. Zumofen, V. Sandoghdar, Efficient coupling of photons to a single molecule and the observation of its resonance fluorescence. *Nature Physics* **4**, 60 (2008).
58. J. Claudon, *et al.*, A highly efficient single-photon source based on a quantum dot in a photonic nanowire. *Nature Photonics* **4**, 174 (2010).
59. B. Pradhan, *et al.*, Gold-Nanorod-Enhanced Fluorescence Correlation Spectroscopy of Fluorophores with High Quantum Yield in Lipid Bilayers. *Journal of Physical Chemistry C* **120**, 25996–26003 (2016).
60. D. Wang, *et al.*, Coherent Coupling of a Single Molecule to a Scanning Fabry-Perot Microcavity. *Phys. Rev. X* **7**, 021014 (2017).
61. K. Matsuzaki, *et al.*, Strong plasmonic enhancement of biexciton emission: controlled coupling of a single quantum dot to a gold nanocone antenna. *Scientific Reports* **7**, 42307 (2017).
62. W. Zhang, M. Caldarola, X. Lu, M. Orrit, Plasmonic Enhancement of Two-Photon-Excited Luminescence of Single Quantum Dots by Individual Gold Nanorods. *ACS Photonics* **5**, 2960–2968 (2018).
63. C. U. Hail, *et al.*, Nanoprinting organic molecules at the quantum level. *Nature Communications* **10**, 1880 (2019).
64. G.-C. Li, Y.-L. Zhang, J. Jiang, Y. Luo, D. Y. Lei, Metal-Substrate-Mediated Plasmon Hybridization in a Nanoparticle Dimer for Photoluminescence Line-Width Shrinking and Intensity Enhancement. *ACS Nano* **11**, 3067–308 (2017).
65. G.-C. Li, Y.-L. Zhang, D. Y. Lei, Hybrid plasmonic gap modes in metal film-coupled dimers and their physical origins revealed by polarization resolved dark field spectroscopy. *Nanoscale* **8**, 7119–7126 (2016).
66. S. T. Jones, *et al.*, The Importance of Excess Poly(N-isopropylacrylamide) for the Aggregation of Poly(N-isopropylacrylamide)-Coated Gold Nanoparticles. *ACS Nano* **10**, 3158–3165 (2016).
67. S. Sacanna, L. Rossi, D. J. Pine, Magnetic Click Colloidal Assembly. *J. Am. Chem. Soc.* **134**, 6112–6115 (2012).
68. S. Sacanna, *et al.*, Shaping colloids for self-assembly. *Nature Communications* **4**, 1688 (2013).
69. M. Kamp, *et al.*, Regiospecific Nucleation and Growth of Silane Coupling Agent Droplets onto Colloidal Particles. *J. Phys. Chem. C* **121**, 19989–19998 (2017).

70. F. Benz, *et al.*, Nanooptics of Molecular-Shunted Plasmonic Nanojunctions. *Nano Lett.* **15**, 669–674 (2015).
71. P. B. Johnson, R. W. Christy, Optical Constants of the Noble Metals. *Phys. Rev. B* **6**, 4370–4379 (1972).
72. J. Yang, J.-P. Hugonin, P. Lalanne, Near-to-Far Field Transformations for Radiative and Guided Waves. *ACS Photonics* **3**, 395–402 (2016).

Author contributions:
MK, BdN, RC, OAS, and JJB conceived of the experiment, which was carried out by MK and BdN. MK developed SPARK synthesis. BdN built the optical setup, with assistance from WMD and JPG. Simulations were performed by NK, MS, RC and OH. CAR performed DFT calculations. SJB prepared the ligand used for SPARK synthesis. OSO, DAW and JH confirmed high SERS efficiencies on separate setups. All authors contributed to analysing and writing up the results.

Competing interests: The authors declare no conflict of interests.

Supporting Materials: This article contains supporting information online at: [intentional blank]